Wave propagation in elasto-plastic granular systems

**Raj Kumar Pal · Amnaya P. Awasthi ·
Philippe H. Geubelle**

Abstract Due to the nonlinear nature of the inter-particle contact, granular chains made of elastic spheres are known to transmit solitary waves under impulse loading. However, the localized contact between spherical granules leads to stress concentration, resulting in plastic behavior even for small forces. In this work, we investigate the effects of plasticity in wave propagation in elasto-plastic granular systems. In the first part of this work, a force–displacement law between contacting elastic-perfectly plastic spheres is developed using a nonlinear finite element analysis. In the second part, this force–displacement law is used to simulate wave propagation in one-dimensional granular chains. In elasto-plastic chains, energy dissipation leads to the formation and merging of wave trains, which have characteristics very different from those of elastic chains. Scaling laws for peak force at each contact point along the chain, velocity of the leading wave, local contact and total dissipation are developed.

Keywords Granular chains · Elasto-plastic spheres · Dissipation rates · Contact law · Wave propagation

R. K. Pal
Department of Mechanical Science and Engineering,
University of Illinois at Urbana-Champaign,
Urbana, IL 61801, USA

A. P. Awasthi · P. H. Geubelle (✉)
Department of Aerospace Engineering,
University of Illinois at Urbana-Champaign,
Urbana, IL 61801, USA
e-mail: geubelle@illinois.edu

1 Introduction

Granular materials have unique wave propagation properties due to the inherently nonlinear nature of their contact. These properties are being envisioned to be exploited in the design of systems for impact protection, blast wave resistance, and those experiencing high pressure load fluctuations. Over the last few decades, extensive studies have been conducted on wave propagation in elastic granular systems [1–4]. These systems are typically modeled by spherical granules characterized by a point contact or a small area of contact, which leads to high stress concentrations in the contact regions. In real systems subjected to high loads, these stress concentrations lead to plastic deformations, and the effects of plasticity become significant. This work aims at a fundamental understanding of the role of plasticity in wave propagation in granular media, and is intended to form the basis of designing systems for stress wave tailoring applications.

Several models have been proposed to extend Hertz's classical theory of elastic contact [5] and account for plastic deformations in contacting spheres. One of the most widely used models for force–displacement in elastic-perfectly plastic contacting spheres is due to Thornton [6]. However, as recently shown by Wang et al. [7], while the Thornton model captures key features of the loading and unloading responses, it substantially under-predicts the experimental force–displacement behavior. The problem of two identical contacting spheres is equivalent to that of a sphere pressing against a rigid flat surface, and the latter problem has been extensively studied in the literature. One of the early examples in this line of work is due to Abbot and Firestone [8], who assumed fully plastic conditions, and thus that the contact area is the area intercepted by the translation of the rigid flat surface. The contact force is obtained by multiplying the contact area with the average contact pressure,

which is assumed to be the hardness. Zhao et al. [9] developed an elasto-plastic model which interpolates smoothly between the elastic (Hertzian) and fully plastic model in a transition region. Vu-Quoc [10] assumed that the contact area can be additively decomposed into elastic and plastic components, and developed an implicit relation between force and displacement using finite element simulations. Kogut and Etsion [11] and Jackson and Green [12] performed extensive finite element simulations and constructed empirical models for contact force–displacement response. It should be noted that the models developed by Vu-Quoc [10] and Kogut et al. [11] operate in relative displacement ranges much smaller than those considered in wave tailoring applications of interest in the present study. Additionally, most of the above models focus only on the loading response. However, to simulate the dynamic response of spherical contacting beads, we need a simple and accurate model to describe initial loading, unloading and reloading.

As shown by Nesterenko [13], a monodisperse elastic chain of uncompressed spherical beads in contact produces compact stress waves called solitary waves when subjected to an impulse loading. The system can be modeled by point masses connected by nonlinear springs, with the force between contacting spheres described by the Hertzian law. While a solitary wave travels unattenuated across the chain in a non-dissipative elastic system, a dissipative system exhibits a very different behavior with the peak force decreasing along the chain. Vergara [14] developed a dissipative model for viscoelastic beads in contact by parametrizing the contact law to include a viscoelastic contribution. Rosas et al. [15,16] studied the dynamics and energy decay in dissipative granular chains where the damping was proportional to the relative velocity of the grains and observed a two wave structure. In Carretero-Gonzalez et al. [17], the authors modeled dissipation by adding a power law of relative velocities to the Hertzian law, with the power law exponent determined from experiments to fit the simulation data. A key observation from that study is the existence of secondary waves below a critical exponent. Most of the studies on wave propagation in granular chains have been conducted on monodisperse elastic chains. Recently, Khatri et al. [18] demonstrated the existence of solitary waves in chains of cylindrical particles. Nguyen and Brogliato [19] studied dispersion in tapered and stepped chains using a multiple impact model. There have also been a few studies in the literature on the dynamics of random contacting spheres and their force propagation and dispersion characteristics [20,21].

The present work attempts to model systematically the effect of plasticity in wave propagation in granular chains by developing a contact force–displacement law and incorporating it into a dynamic model of wave motion in a 1-D chain of elastic-perfectly plastic spheres. In the first part of this paper, finite element simulations are used to develop force–displacement laws for a wide range of material properties and a large relative displacement range, under both loading and unloading conditions. This law, first derived for identical spheres in contact, is then extended to incorporate spheres of distinct radii made of the same material. The contact force–displacement law is then used to study the dynamic response of uncompressed spherical beads in contact, analyze the distinct characteristics of plastic waves, and characterize the decay in peak force and wave velocity. That aspect of the study includes the development of scaling laws for energy dissipation in the granular system.

2 Contact force displacement model

The objective of this section is to construct a model to compute the contact force for a given relative displacement between the centers of two contacting spheres. Detailed finite element simulations are performed to obtain the force–displacement solution for two rate-independent elastic-perfectly plastic spheres in contact, and this solution is compared with experimental data [7] and with the Thornton model [6]. The limitations of the Thornton model are presented, and a new model having a wider applicability is constructed based on the finite element solutions.

2.1 Finite element simulations

The boundary value problem of two elastic-perfectly plastic spheres under contact is presented schematically in Fig. 1a, together with a close-up of the mesh in the vicinity of the contact surface. To extract the relation between the contact force and the relative displacement between the center of the spheres, two half-spheres in contact are considered in the problem setup. A static, axisymmetric finite element structural analysis is performed to extract the force–displacement data for a rate-independent material, based on the assumption that the time scale of dynamic wave propagation across the chain is much larger than that of elastic wave propagation within the sphere [13]. One end of a half sphere is fixed, while a uniform vertical displacement is imposed on the entire flat surface of the other half-sphere. The flat surfaces of both the half-spheres are free to move in the horizontal direction, while the curved surfaces are traction free. Since the spheres in this first set of simulations are identical, the bottom sphere could be replaced by a rigid flat surface. However, we use two half-spheres since spheres of dissimilar radii are later modeled using the same problem set-up.

The finite element analysis software ABAQUS is used to solve the above problem. First-order axisymmetric quadrilateral (CAX4R) and triangular (CAX3) elements are used with the master–slave contact algorithm at the contact surfaces. The half-spheres are meshed with approximately 72,000

(a)

(b)
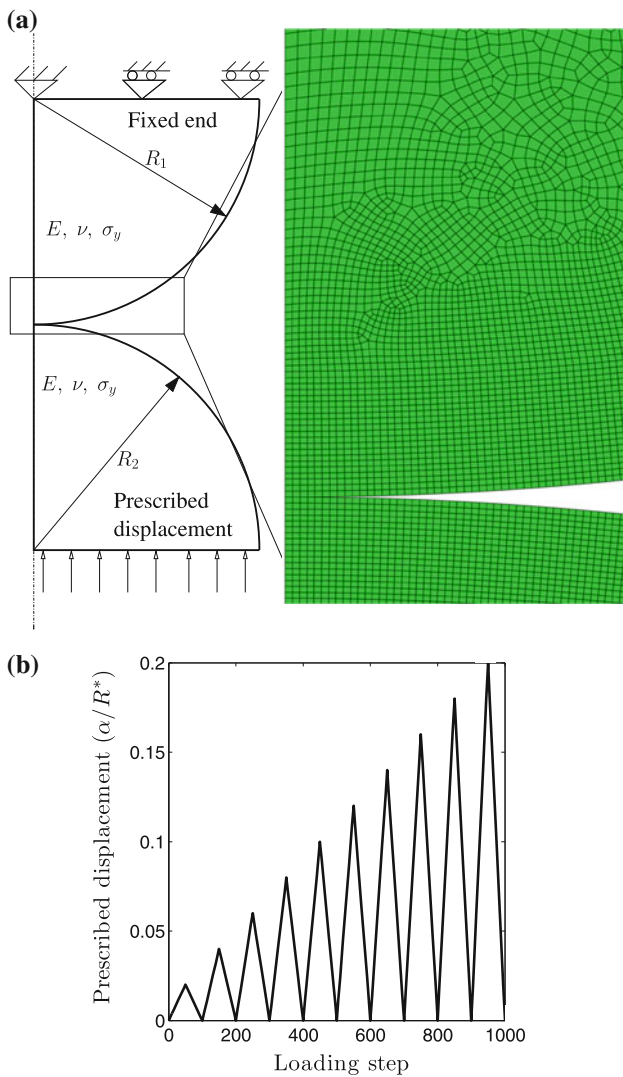
Fig. 1 Problem description. **a** A schematic of the axisymmetric problem with boundary conditions. A close-up of the mesh at the contact surface is also shown, emphasizing the fine structured mesh used in the vicinity of the contact surface. **b** Variation of prescribed displacement over the loading history used in the simulation

elements, with a fine layer of structured mesh along the contact surface, and an unstructured mesh in the remaining domain. To match the experimental results described later, the radii of the spheres are chosen to be $3/8''$ (4.76 mm). The Young's modulus ($E = 115$ GPa) and Poisson ratio ($\nu = 0.30$) are chosen to correspond to brass, although the results are presented hereafter in a non-dimensionalized way. Finite element simulations are performed for a range of yield strength values from 400 to 1,500 MPa. Coulomb friction is introduced between the contact surfaces with a friction coefficient 0.30 to keep the solution symmetric with respect to the contact surface. In the absence of friction, the numerical solution deviates from symmetry and becomes unstable at large relative displacements. The presence of friction stabilizes the

solution, but the solution itself is found to be independent of the specific value of a sufficiently large friction coefficient. Large deformation static solutions are performed with loading and unloading cycles as shown in Fig. 1b. In that figure, the prescribed displacement α is normalized by R^*, which is the effective radius of the two spherical surfaces in contact given by

$$R^* = \frac{R_1 R_2}{R_1 + R_2}, \tag{1}$$

where R_1 and R_2 are the radii of the two contacting surfaces. The total contact force F is computed by summing the reaction forces acting on all the nodes at the top or bottom flat surfaces of the half-spheres.

2.2 Force–displacement model

2.2.1 Loading

The force–displacement data extracted from finite element solution is normalized as follows. The displacement α between the sphere centers is normalized by α_y, the displacement at the onset of yielding given by Thornton [6]

$$\alpha_y = \frac{\pi^2}{4} \left(\frac{p_y}{E^*}\right)^2 R^*. \tag{2}$$

In (2), E^* is the effective modulus of the solids in contact, defined as

$$\frac{1}{E^*} = \frac{1 - \nu_1^2}{E_1} + \frac{1 - \nu_2^2}{E_2} = \frac{2\left(1 - \nu^2\right)}{E},$$

and p_y is the contact yield stress, which is related to the material yield strength σ_y by $p_y = 1.60\,\sigma_y$ for materials with Poisson ratio $\nu = 0.30$ [5]. This relation is found to be consistent with our numerical solutions, where yielding starts when the peak pressure on the contact surface reaches p_y. The contact force F is normalized by F_y, the force at the onset of yield obtained from Hertzian law [5] as

$$F_y = \frac{4}{3} E^* R^{*1/2} \alpha_y^{3/2}. \tag{3}$$

Figure 2 shows the normalized force–displacement data extracted from the finite element solution for $\sigma_y = 550$ MPa. The monotonic curve starting from the origin corresponds to plastic loading, while the steeper curves originating from this loading curve correspond to unloading and reloading. Also shown in the figure is the Hertzian solution, which is much steeper, and deviates from the elasto-plastic solution for small values of contact force, emphasizing the key role played by plasticity. For the material properties used in this study, the force required to cause yielding F_y (3) is quite small and is around 5 N, which corresponds to unity in Fig. 2. Due to residual plastic deformations for contact
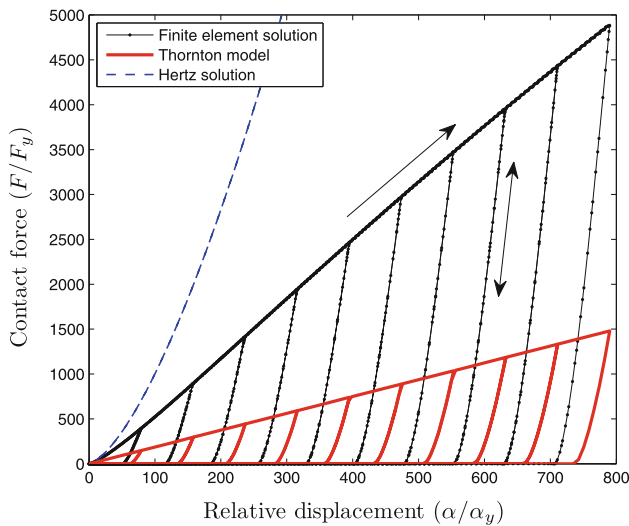
Fig. 2 Force–displacement response of two contacting elastic-perfectly plastic spheres for the loading profile in Fig. 1b. The *monotonic curve* starting from the origin corresponds to plastic loading, while the *steeper curves* correspond to elastic unloading and reloading. Also shown are the elastic (Hertzian) solution and the prediction provided by the Thornton model [6] for the same system and loading conditions

Fig. 3 Pressure distribution along the contact surface for identical elasto-plastic spheres, evaluated using FEA for ten values of the applied relative displacement α. For high α, the pressure is almost uniform over the contact surface. The *dotted line* shows the pressure distribution predicted by the Thornton model for $\alpha/R^* = 0.20$

forces exceeding F_y, a displacement is observed when the force goes to zero during unloading. Furthermore, subsequent reloading follows the unloading curve until the force level at which unloading started, implying that the unloading and reloading are elastic.

The Thornton model [6] predicts the following linear variation of force with relative displacement

$$F = F_y + \pi \sigma_y R^* \left(\alpha - \alpha_y \right) \tag{4}$$

in plastic loading, and it assumes the following power law in unloading and elastic reloading:
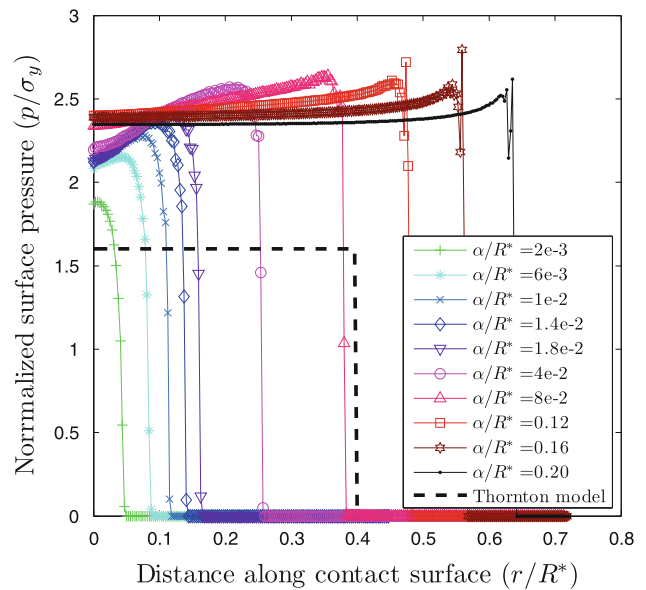
$$F = \frac{4}{3} E^* R_p^{*1/2} \left(\alpha - \alpha_p \right)^{3/2}, \tag{5}$$

where

$$R_p^* = \frac{4E^*}{3F_{\max}} \left(\frac{2F_{\max} + F_y}{2\pi \sigma_y} \right)^{3/2} \tag{6}$$

is the effective radii at contact during unloading [6], $F_{\max}$ is the contact force at the onset of unloading and α_p is the residual displacement, obtained by satisfying Eqs. (4) and (5) at the onset of unloading. The Thornton model is shown for comparison in Fig. 2. Though qualitatively similar to the finite element solution, it clearly under-predicts the contact force during plastic loading.

To explain this discrepancy, one should examine in detail the two key contributions to the contact force $F = \bar{p}A$, that is, the average contact pressure $\bar{p}$ and the contact area A. Figure 3 shows the variation of contact pressure (traction stress in the axial direction) along the contact surface. The

numerical solution shows the pressure to rise beyond p_y and reach a maximum value of about 2.5 σ_y. Similar trends have been observed by Jackson and Green [12], who related the contact pressure to the hardness of the material. For large relative displacements, the pressure is nearly constant along the contact surface, allowing characterization of the surface contact pressure by an average value $\bar{p}$.

Figure 4 shows the variation of the normalized average pressure $\left(\bar{p}/\sigma_y \right)$ with applied relative displacement α for multiple values of material yield strengths, with $\gamma = \sigma_y/E^*$. As shown there, the average pressure increases sharply to a constant value as α increases and we thus construct a simple model that transitions between the two regimes. At the onset of yielding, the pressure distribution along the contact surface is elliptic [5], as described by the Hertzian solution and the average surface pressure is evaluated as

$$\bar{p} = \frac{1}{\pi a^2} \int_A p_y \sqrt{1 - \left(\frac{r}{a} \right)^2} \, dA = \frac{2}{3} p_y = 1.07 \sigma_y, \tag{7}$$

where a and A are the contact radius and area, respectively. An exponential correction in the transition regime from elastic to larger displacement fully plastic regime leads to the following relation:

$$\frac{\bar{p}}{\sigma_y} = c_1 - (c_1 - 1.07) \exp\left(-c_2 (\tilde{\alpha} - 1) \right), \tag{8}$$
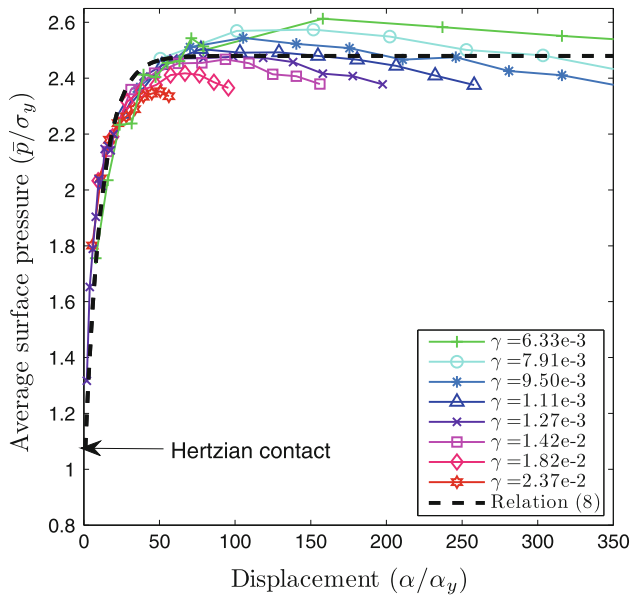
Fig. 4 Average contact pressure ($\bar{p}$) versus applied displacement for eight values of the normalized yield stress $\left(\gamma = \sigma_y/E^*\right)$. The variation of normalized average pressure with displacement seems to follow a single law for different yield strengths. For small displacements, there is a transition from the elastic Hertzian solution to the almost constant value observed for large relative displacements

Fig. 5 Contact area versus displacement for eight values of yield stress $\left(\gamma = \sigma_y/E^*\right)$. When normalized by their respective values at the onset of yield, the area-displacement curves collapse to a single curve

where $c_1 = 2.48$, $c_2 = 0.098$ and $\tilde{\alpha} = \alpha/\alpha_y$ is the normalized displacement. Relation (8) is shown as a dashed curve in Fig. 4.
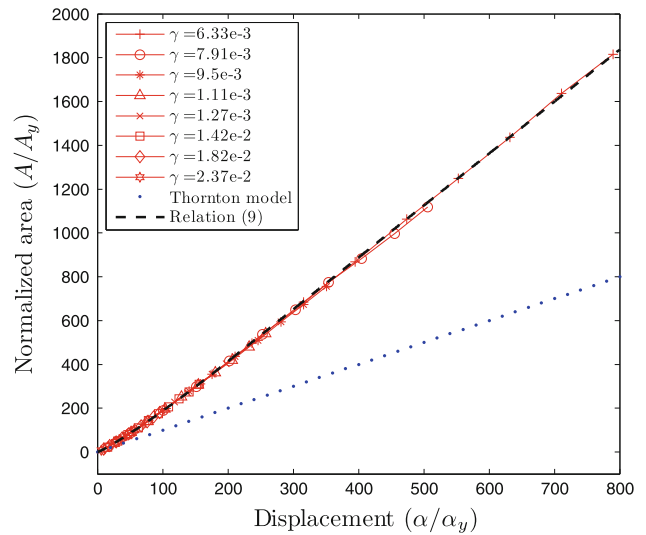
To complete the force–displacement relation in loading, we now characterize the evolution of the contact area A with the applied displacement α. The contact radius a can be extracted numerically by capturing the point along the contact surface where the pressure p drops to zero. The contact area $\left(A = \pi a^2\right)$ is normalized by the contact area at the onset of yielding A_y, obtained from Hertzian contact law as

$$A_y = \pi a_y^2 = \pi R^* \alpha_y, \tag{9}$$

where R^* and α_y are given by (1) and (2), respectively. Figure 5 presents the contact area distribution for different values of yield strength σ_y, showing the existence of a single 'master' curve. For all displacements, the Thornton model [6] assumes a linear variation of contact area with displacement following the Hertzian law. The numerical results obtained in this study show that the contact area indeed varies almost linearly, but with a different slope than that assumed by the Thornton model. For small displacements after the onset of yielding, the contact area follows a power law in the transition regime as

$$\tilde{A} = \frac{A}{A_y} = \begin{cases} \tilde{\alpha}^{c_3}, & \text{if } \tilde{\alpha} < \alpha_0, \\ (c_4\tilde{\alpha} - c_5), & \text{otherwise} \end{cases} \tag{10}$$

where $c_3 = 1.14$, $c_4 = 2.37$, $c_5 = 59.96$ and $\alpha_0 = 177.6$ is the displacement $\tilde{\alpha}$ where the power law and linear fit curves intersect. Relation (10) is shown as a dashed curve in Fig. 5.

The Thornton model [6] assumes that the maximum contact pressure does not increase beyond p_y, the maximum contact pressure along the surface at the onset of yield. However, the numerical solution (Fig. 3) shows the pressure increasing beyond p_y and reaching a maximum of about $2.5\sigma_y$. The difference in the plastic loading regime between the numerical solution and Thornton model thus arises from two factors: the contact pressure is about 2.31 times the surface contact pressure assumed in the Thornton model, and the contact area is about 2.1 times the contact area assumed in the Thornton model. Recently, Wang et al. [7] used a modified Thornton model, where the contact yield stress is related to the yield strength as $p_y = f\sigma_y$, where f is a fitting parameter derived from matching a Thornton model curve with the maximum load levels attained by experiments. Thus, a combination of these two effects gives a factor close to 4.7, the parameter used by Wang et al. [7] in the modified Thornton model. Furthermore, both our data-fitted model and the Thornton model are linear for large displacements, and hence a modified Thornton model [7] gives a good fit in the loading regime.

2.2.2 Unloading

The unloading response of the contacting spheres is characterized by the displacement $\alpha_{\max}$ and corresponding force $F_{\max}$ at the onset of unloading. Since the unloading and subsequent reloading curves overlap (*cf.* Fig. 2), unloading is a completely elastic process. Let α_R be the residual displacement at zero contact force. For a given unloading curve, the displacement can be scaled as

$$\alpha_s = \frac{\alpha - \alpha_R}{\alpha_{\max} - \alpha_R}, \tag{11}$$
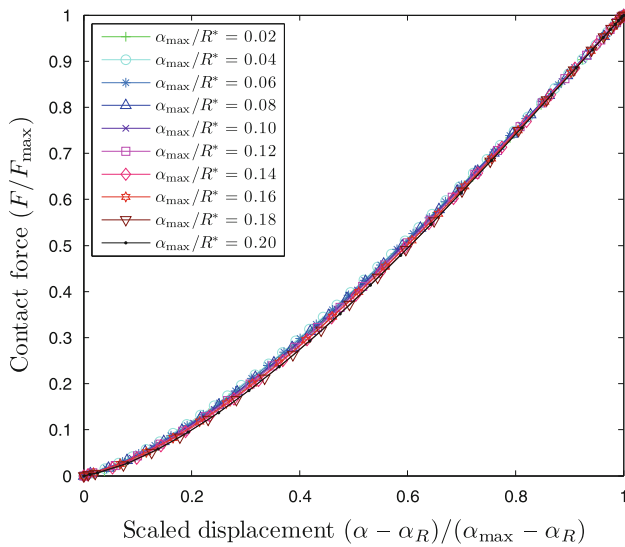
Fig. 6 Unloading *force–displacement curves* obtained for different onsets of unloading characterized by the maximum previously achieved value of displacement α_{max} and force F_{max}

Fig. 7 Residual displacement (α_R) versus displacement at onset of unloading (α_{max}). The displacements are normalized by displacement at onset of yield (α_y). All curves collapse on a single "master" curve denoted by the *solid curve*
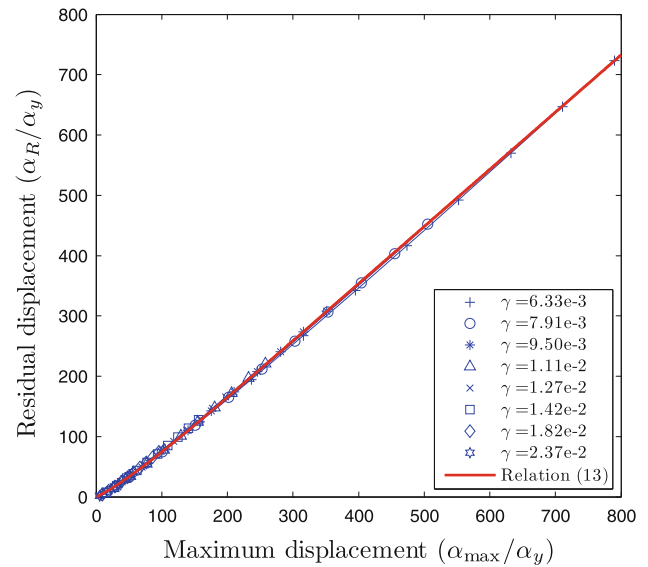
while the force is scaled by F_{max}. As shown in Fig. 6, the normalized unloading contact curves obtained numerically for ten values of α_{max} collapse to a single curve. Unloading curves for other yield strength values also show the same behavior. Thus a single law suffices to describe the unloading response in the form

$$\frac{F}{F_{max}} = \left(\frac{\tilde{\alpha} - \tilde{\alpha}_R}{\tilde{\alpha}_{max} - \tilde{\alpha}_R}\right)^n, \tag{12}$$

where n is the unloading exponent, and all displacements have been normalized by α_y. To compute the force during unloading using (12), we need to determine the residual displacement α_R for a given displacement at the onset of unloading α_{max}. As shown in Fig. 7, the variations of residual displacement $\tilde{\alpha}_R = \alpha_R/\alpha_y$ with maximum displacement $\tilde{\alpha}_{max}$ for different yield strengths all follow a single 'master' curve. A linear fit captures the variation well at larger displacements, but it deviates for small displacements. There is a transition regime between zero residual displacement at the onset of yield and the linear variation regime at large displacements. Again, an exponential correction is added to capture the variation in this transition regime:

$$\tilde{\alpha}_R = \frac{\alpha_R}{\alpha_y} = c_6 \tilde{\alpha}_{max} - c_7 + (c_7 - c_6)$$
$$\exp\left(-c_8 \left(\tilde{\alpha}_{max} - 1\right)\right), \tag{13}$$

where $c_6 = 0.95$, $c_7 = 25.94$ and $c_8 = 0.015$. The exponent for all yield strength values and for all unloading points in the plastic regime is found to vary between 1.30 and 1.42. We therefore use a constant value of $n = 1.35$ and observe that this value fits the finite element solution data with reasonable accuracy for all regimes and for a wide range of yield strength

values. It should be noted that this value is slightly inferior to the value $n = 1.5$ assumed in the Thornton model (5).

2.2.3 Verification and validation

The complete force–displacement law for the plastic loading regime is thus

$$F = \sigma_y A_y \left(2.48 - 1.41 \exp\left(-0.098\left(\tilde{\alpha} - 1\right)\right)\right) \tilde{A}, \tag{14}$$

with $\tilde{A}$ given by

$$\tilde{A} = \begin{cases} \tilde{\alpha}^{1.14}, & \text{if } \tilde{\alpha} < 177.6, \\ (2.37\tilde{\alpha} - 59.96), & \text{otherwise} \end{cases} \tag{15}$$

for the plastic loading regime and

$$F = F_{max}\left(\frac{\alpha - \alpha_R}{\alpha_{max} - \alpha_R}\right)^{1.35} \tag{16}$$

for unloading and elastic reloading regimes, with the residual displacement α_R given by

$$\alpha_R = 0.95\alpha_{max} - 25.94\alpha_y$$
$$+ 25.0\alpha_y \exp\left(-0.015\left[\tilde{\alpha}_{max} - 1\right]\right). \tag{17}$$

Figure 8 shows the comparison of numerical results with the model described by (14)–(17) for materials of yield strength $\sigma_y = 400$, 500 and 800 MPa. The model matches the finite element solution accurately for small and moderate displacements, while for large displacements, the force is slightly over-predicted. The maximum error in the model compared to the finite element solutions is found to be about 6 %. The force predicted by the model starts to deviate from
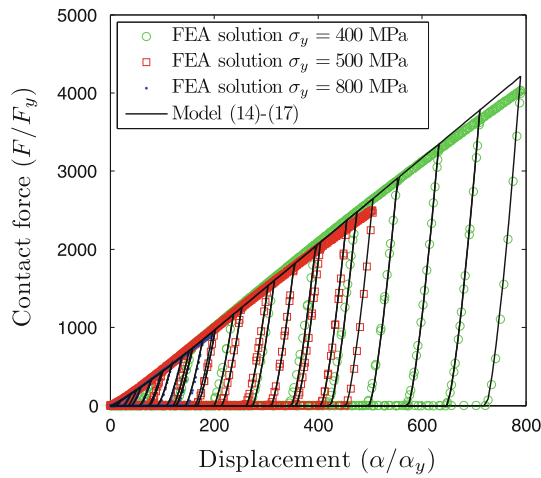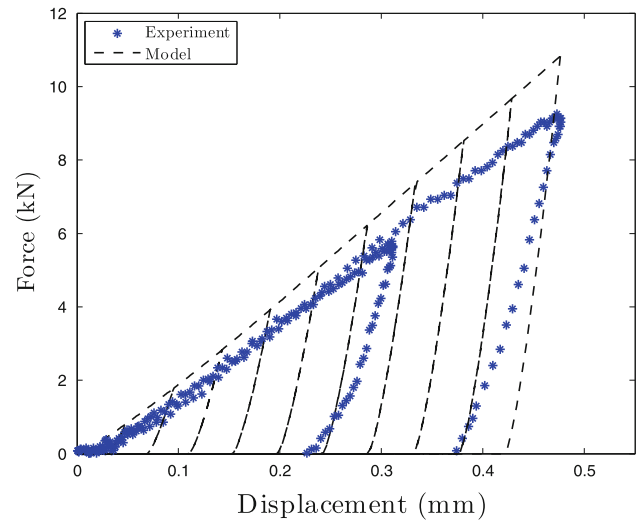
Fig. 8 Comparison between the numerically obtained force–displacement data (*symbols*) with the model described by Eqs. (14), (16) and (17)

Fig. 9 Comparison of model with experimental data [7]. The experimental system comprises of brass beads ($R = 4.76$ mm, $E = 115$ GPa, $\nu = 0.30$, $\sigma_y = 550$ MPa), and the loading and unloading are done quasi-statically. There is some disagreement stemming from the elastic-perfectly plastic model assumption in the simulation

the numerical solution for large displacements due to the average contact pressure falling from the constant value, as seen in Fig. 4, and this is attributed to the effect of change in curvature at large deformations. Jackson et al. [12] report similar trends, where the contact pressure reaches a peak value before progressively decreasing.

Figure 9 shows a comparison of the data fitted model for brass with $\sigma_y = 550$ MPa with experimental data for quasi-static loading of two brass half-spheres [7]. There is some disagreement between the experimental data and our model, arising due to an uncertainty of ± 50 MPa in the actual value of yield strength σ_y used in experiments. The low slope of the loading curve at small displacements for the experimental curve is attributed to the transition regime from elastic to plastic behavior for brass, in contrast to the elastic-perfectly plastic model assumed for finite element simulations. The deviation of experimental data from the model in the unloading part is attributed to the presence of hardening in the brass spheres, which leads to a less steep unloading response.

2.3 Contact law for spheres of different radii

Finite element simulations with contacting spheres of different sizes are also performed, with the radii ratio ranging from 1.5 to 4. The problem schematic and the boundary conditions are the same as in Fig. 1a. The same prescribed displacement (shown in Fig. 1b) is applied to all systems, and the force–displacement response is shown in Fig. 10. The curves completely overlap for small to moderate displacements. At large displacements, the loading curves for dissimilar radii begin to deviate from those for identical spheres. This is attributed to two phenomena: firstly, at higher dis-
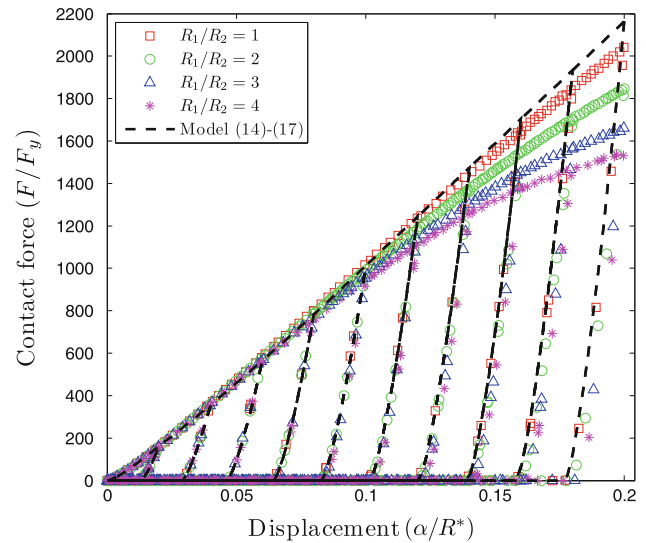
Fig. 10 Force–displacement data extracted from finite element solutions for contacting spheres of different radii. For small and moderate displacements, the normalized curves overlap, for large displacements, the entire smaller sphere yields, and the *force–displacement curves* begin to deviate

placements, the entire smaller sphere becomes plastic and this leads to the material becoming softer. Secondly, similar to the effect of average contact pressure decreasing for identical spheres, there may be geometric softening causing the loading curve to deviate from the model and from the identical spheres finite element solution for large relative displacements. Thus the force–displacement model [Eqs. (14)–(17)]

developed earlier for spheres of same radius can be directly used for elastic-perfectly plastic spheres of distinct radii in contact, after appropriate normalizations.

3 Wave propagation in elasto-plastic granular chains

3.1 Problem statement

The contact law developed in the previous section [Eqs. (14)–(17)] is now used to study the response of a semi-infinite chain of elastic-perfectly plastic spherical beads subjected to a force impulse at one end. The chain is represented by a series of point masses connected by nonlinear springs with stiffness defined by the force–displacement contact law. The equation of motion of the ith bead along the chain can be written as

$$m_i \ddot{u}_i = F_{i-1,i}\left(\alpha_{i-1,i}\right) - F_{i,i+1}\left(\alpha_{i,i+1}\right). \tag{18}$$

with $F_{i,j}$ denoting the contact force between spheres i and j and

$$\alpha_{i-1,i} := \begin{cases} u_{i-1} - u_i, & \text{if } u_{i-1} > u_i \\ 0, & \text{otherwise.} \end{cases} \tag{19}$$

For the first bead, the equation of motion is

$$m_1 \ddot{u}_1 = f(t) - F_{1,2}\left(\alpha_{1,2}\right), \tag{20}$$

where $f(t)$ denotes the applied impulse excitation load and is given by

$$f(t) = f[P, T](t) = \begin{cases} P \sin\left(\dfrac{\pi t}{T}\right), & \text{if } 0 \le t \le T \\ 0, & \text{otherwise.} \end{cases} \tag{21}$$

For a given amplitude P and time T of loading, the total impulse imparted to the first bead is $I = 2PT/\pi$. A fourth-order Runge Kutta solver is used to simulate the dynamic response of the system with a time step of 5×10^{-9}s. The solutions are presented in a nondimensional fashion, with the wave velocity v and impulse I being normalized as:

$$\tilde{v} = v\tau/R^* \tag{22}$$
$$\tilde{I} = I/E^* R^{*2}\tau, \tag{23}$$

where τ is the intrinsic time-scale associated with the elastic sphere system,

$$\tau = \sqrt{\frac{\pi \rho R^{*2}}{4E^*}}. \tag{24}$$

3.2 General characteristics of waves

The tests listed in Table 1 are performed on brass spheres having density $8{,}500$ kg/m^3, Young's modulus 115 GPa, Poisson ratio 0.30, yield strength 550 MPa and diameter

4.763 mm $(3/8'')$. Dynamic simulations are performed on both elastic and elasto-plastic chains, with elastic chains modeled by the Hertz contact model for all forces, and the time evolution of the peak force at each contact point is studied for both cases. Figure 11 shows the time history of the force acting at a few contact points for $P = 20$ kN and $T = 10\,\mu$s, while Fig. 12 shows the x-t plot of force at the contact points over the entire simulation. To avoid overlap, the elastic response is plotted shifted from the origin in Fig. 12, starting from the twentieth contact. In an elastic chain, a solitary wave forms in the first few beads and propagates unattenuated at a constant speed along the chain, with a constant peak force and a wavelength approximately equal to five sphere diameters.

In the elasto-plastic case, multiple waves pass through each contact point as wave-trains form and waves interact. The amplitude of the leading wave also decreases as the wave progresses along the chain due to dissipation. Figure 11 also shows that, in the plastic case, the maximum force at a contact point does not always correspond to the first peak force experienced by the bead. The force amplitude and the speed of the leading wave decrease rapidly, as the leading wave operates in the plastic loading regime of the beads. As seen in Fig. 12, a continuous stream of trailing secondary waves forms behind the leading wave. These trailing waves primarily operate in

Table 1 Force and impulse applied to the granular chain

Amplitude, P (N)				Impulse, I (Ns)
2×10^5	2×10^4	1×10^4	2×10^3	1.27×10^{-1}
5×10^5	1×10^5	1×10^4	5×10^3	6.37×10^{-2}
2×10^4	2×10^3			1.27×10^{-2}
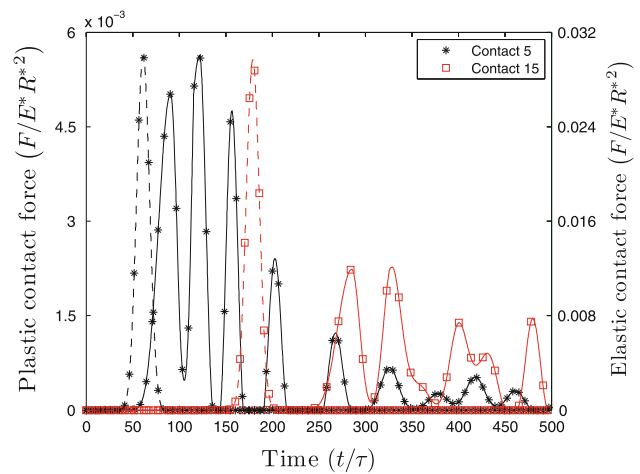
Fig. 11 Force history at two contacts along the elastic (*dotted curves*) and elasto-plastic (*solid curves*) chains. In the elastic case, a single solitary wave of constant amplitude propagates, while the plastic chain is characterized by a wave train of rapidly decaying amplitude
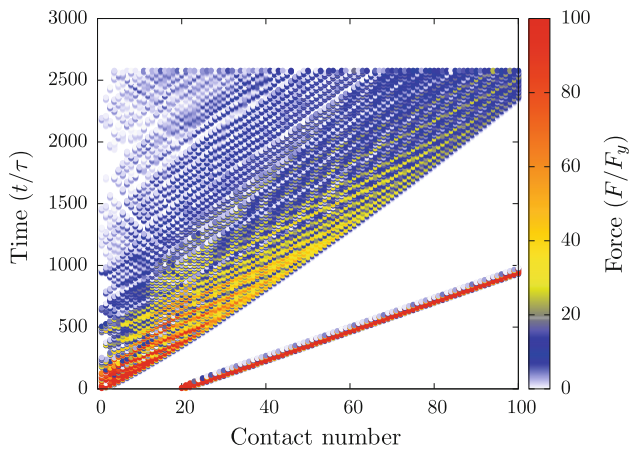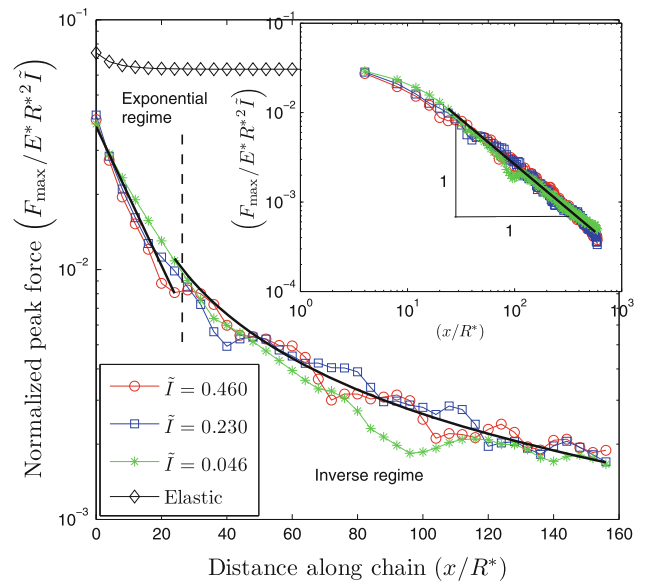
Fig. 12 *x–t* plot of compressive force at each contact point along an elastic and elasto-plastic chain. The elastic response is plotted shifted from the origin, and consists of a single solitary wave propagating at a constant speed and amplitude. In contrast, wave trains form and the wave-front speed and peak force decrease with distance in the elasto-plastic case

Fig. 13 Force decay along the chain consisting of two regimes. In the first regime, the force decay is exponential. The trailing waves catch up soon, and the second regime having an inverse power law decay rate starts. The inset shows the response of a longer chain on a log–log scale. The elastic response denoted by *diamond symbols* is shown for comparison

the elastic loading regime as their peak contact force is lower than the previously attained maximum contact force due to the passage of the leading wave. At some contacts, the trailing waves cause dissipation when their peak force exceeds the maximum force attained by the leading wave. The wave speed is proportional to the slope of the force–displacement curve, and the elastic unloading part has a higher slope than the plastic loading part at high forces. Thus, trailing waves with a sufficient force amplitude travel faster than the leading wave and eventually merge with the leading wave at the front. This wave merging leads to an increase in amplitude of the wave and thus the peak force at contact points does not vary monotonically with distance along the chain.

3.3 Force and velocity characterization

The peak force decays rapidly along the elasto-plastic chain and Fig. 13 shows that the decay rate has two distinct regimes. In the first regime, which comprises of the first few contacts, the energy dissipation is due to a single decaying wave traveling down the chain, and the decay rate of the amplitude of this leading wave with distance along the chain is exponential. The single leading wave travels some distance until the faster moving trailing waves merge with it, and the second regime starts. In the second regime, wave interaction and merging occurs and the dissipation at a contact happens due to multiple waves. The peak force is observed to be inversely proportional to the distance along the chain in this regime. Also shown in the figure is the response of an elastic chain subjected to an impulse $I = 0.127$ Ns and amplitude $P = 20$ kN. We observe that, in the elastic case, the

decay associated with the creation of a solitary wave is much smaller than the plastic case and happens over a much smaller distance from the point of impact. To characterize the decay rate of the first leading wave in the plastic case, we consider a loading case with a peak loading amplitude and loading time of $2,000$ N and $10\,\mu s$, respectively. For this loading, the first trailing wave merges with the leading wave at the 21st contact point. Using this solution, the following characterization for the peak force decay of the leading wave is obtained:

$$\frac{F_{\max}}{E^* R^{*2} \tilde{I}} = a \exp\left(-bx/R^*\right), \tag{25}$$

where $a = 3.74 \times 10^{-2}$ and $b = 0.256$. For the second regime, the following relation is obtained for the peak force variation along the chain:

$$\frac{F_{\max}}{E^* R^{*2} \tilde{I}} = \frac{C}{x/R^*}, \tag{26}$$

where $C = 0.268$. Figure 13 shows the peak force variation and the exponential and inverse law curves for three values of the applied impulse.

We now study the response of a long chain subjected to different loading amplitudes P and impulses I (listed in Table 1) and characterize the peak force and wave velocity. The top curves in Fig. 14 show the peak force along the chain for different loading amplitudes, but with the same initial input impulse. When the loading time T is short, the
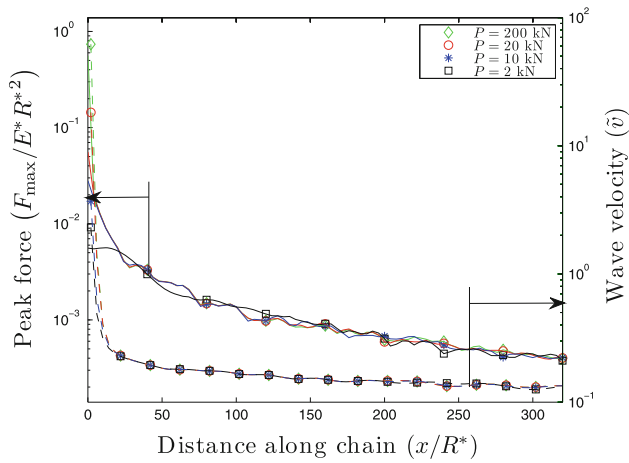
Fig. 14 Peak force (*top curves*) and wave velocity (*bottom curves*) variation along the chain for the same input impulse. The responses for distinct loading amplitudes overlap, implying that both peak force and wave velocity variations are functions of total impulse only

Fig. 15 Wave velocity along the chain. When normalized by $\tilde{I}^{1/6}$, the responses for distinct input impulses collapse to a single curve away from the first few beads. The *inset* shows the variation on a log–log scale and the two distinct propagation regimes. In the second regime, the velocity variation follows a power law with exponent $-1/5$

responses are observed to be almost identical for systems subjected to the same initial impulse. Since waves merge in the second regime, the location of the peak contact force along the chain varies discontinuously with time. To characterize the wave velocity of elasto-plastic waves, the notion of a *leading wave velocity* is introduced as the time taken for the leading front or disturbance to travel between two adjacent contacts. The lower curves in Fig. 14 show the leading wave velocity for chains subjected to different loading amplitudes and a fixed impulse. Once again, the curves overlap and the response is independent of loading amplitude.

Figure 13 shows the peak force decay for systems subjected to different impulses I, but with the same loading amplitude P. When normalized by their corresponding input impulses, the responses corresponding to distinct impulses overlap in both the exponential and inverse decay regimes. The inset in Fig. 13 shows that the responses continue to overlap for even very long chains. Figure 15 shows the spatial dependence of the wave velocity for systems subjected to distinct impulses I with the same loading amplitude P. After scaling the wave velocity by a power of the impulse $\tilde{I}^{1/6}$, the curves overlap in the second regime in which the wave velocity is observed to scale with distance as $x^{-1/5}$. Since the peak force $F_{\max}$ follows an inverse law in this region, it follows that the leading wave velocity scales as $F_{\max}^{1/5}$ along the chain. This result is in contrast with the $F_{\max}^{1/6}$ dependence of the solitary wave speed in elastic granular chains [2]. Thus the peak force and velocity responses scale with functions of impulse $\tilde{I}$ and $\tilde{I}^{1/6}$, respectively, and do not depend on the loading amplitude.
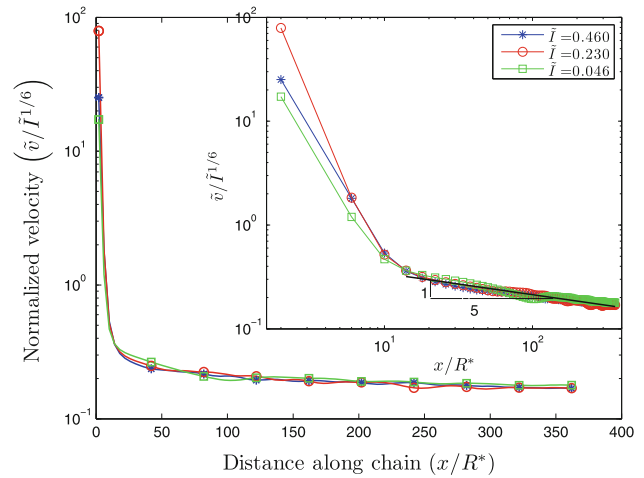
3.4 Energy dissipation

The dissipation along the chain, both at an individual contact level and for the entire chain, is characterized using the peak force relations developed above. At a contact point attaining a peak force $F_{\max}$, the dissipated energy E_{dis} is equal to the difference in areas under the loading and unloading force–displacement curves for this value of $F_{\max}$. Equation (31) in the appendix gives the energy dissipation expression as a function of the maximum displacement $\alpha_{\max}$ for the model constructed in the previous section. To compute the energy dissipation along the entire chain using the peak force decay rates [Eqs. (25) and (26)], a simple approximation is constructed relating the energy dissipation and force at a contact. Since the contact force varies linearly with displacement for large displacements in the loading regime [Eqs. (14) and (15)], the area under the loading curve can be approximated by a quadratic function of the force. For unloading, since the residual displacement α_R varies linearly with the displacement at the start of unloading $\alpha_{\max}$ for large displacements [Eq. (17)], the area under the unloading curve also varies quadratically with force. Hence the energy dissipation at a given contact can be approximated by a quadratic function:

$$\tilde{E}_{dis} = \frac{E_{dis}}{F_y \alpha_y} = d_0 + d_1 \tilde{F}_{\max} + d_2 \tilde{F}_{\max}^2, \tag{27}$$

where $\tilde{F}_{\max} = F_{\max}/F_y$, $d_0 = 1.23 \times 10^{-4}$, $d_1 = -3.63 \times 10^{-7}$ and $d_2 = 1.86 \times 10^{-8}$ for the model described by (14)–(17). This approximation is found to be in good agreement with the exact expression given by (31).

Using these relations, we can evaluate the energy dissipated at a contact located distance $\tilde{x} = x/R^*$ along the chain, after all the waves have passed. In the first regime, the exponential force decay rate (25) leads to

$$\tilde{E}_{dis} = d_0 + d_1 a \tilde{I} \exp(-b\tilde{x}) + d_2 \left(a\tilde{I} \exp(-b\tilde{x})\right)^2, \quad (28)$$

while in the second regime, the spatial variation of the energy dissipation is given by

$$\tilde{E}_{dis} = d_0 + d_1 \frac{C\tilde{I}}{\tilde{x}} + d_2 \left(\frac{C\tilde{I}}{\tilde{x}}\right)^2, \quad (29)$$

using the inverse force decay rate (26). As apparent in Fig. 13, the second regime starts from about the seventh contact point. In the numerical simulations performed in this study, the second regime is observed to start between the sixth and tenth contact points. Therefore, to compute the dissipation at any contact point along the chain, the transition between the first and second regimes is fixed at an average value of $\tilde{x}_t = x_t/R^* = 28$, that is, the seventh contact point.

The total energy dissipated E_{tot} along a chain is obtained by summing the dissipation at each contact point as:

$$E_{tot} = \sum_{i=1}^{N} E_{dis}(x_i) \approx \frac{1}{2R} \int_{x_1}^{x_N} E_{dis} dx. \quad (30)$$

The above integral is evaluated using Eqs. (28) and (29) and is provided in the Appendix [Eq. (32)]. Figure 16 shows the total energy dissipation along the chain for different impulses, obtained from numerical simulations and the predicted energy dissipation using relation (30). For lower input

Fig. 16 Total dissipation versus distance. The simulation results are compared with the predicted results, obtained from (32) and they are in good agreement

impulses, the total energy dissipated along the chain is described accurately by the above equations while, for higher impulses, the error is less than 6%. This error is due to the model assuming the transition from exponential to inverse decay regime for peak force to always happen at a fixed point for all impulses. A large fraction of the energy is dissipated in the first regime, where the forces are high and the decay rate is exponential.
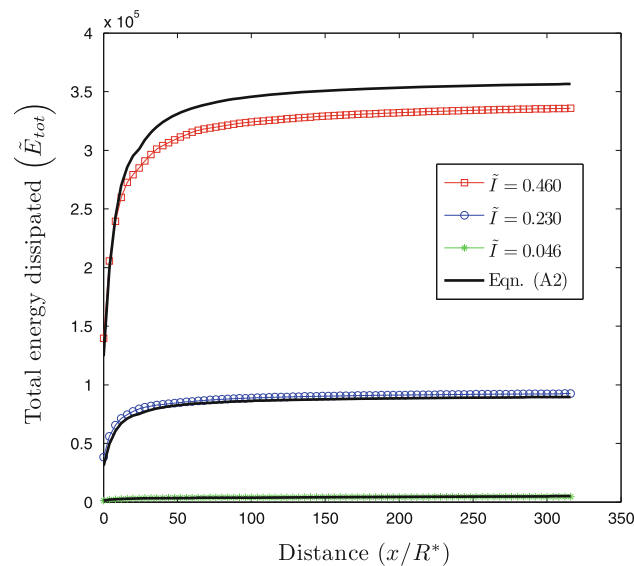
4 Conclusions

In the first part of this work, finite element analyses of contacting elastic-perfectly plastic spheres of the same material, with identical or distinct radii have been performed. Simulations for a wide range of material properties and for a large displacement range have been conducted. Scaling relations and numerical fits have been extracted to develop a 9-parameter model and describe the contact force displacement relation for loading, unloading and reloading of elasto-plastic spheres.

In the second part, Hertzian law and new elasto-plastic contact model have been used to perform dynamic simulations on semi-infinite elastic and elasto-plastic granular chains, with a force impulse applied at one end. In an elastic chain, a solitary wave propagates unchanged, while in an elasto-plastic chain, the wave amplitude decreases due to dissipation, and there is formation and interaction of wavetrains. For small loading times, the peak force and wave velocity along the chain depend only on the input impulse and the scaling laws for these quantities have been determined. The force decay has two distinct regimes, the first regime has an exponential decay rate due to the dissipation associated with the leading wave, and the second regime has an inverse decay rate, during merging and interaction of multiple waves. Finally, the dissipation in these elasto-plastic chains has been characterized for different impulses.

Appendix: Energy dissipation

The energy dissipation at a contact is given by the expression (31), where $\alpha = \alpha_{max}$ is the maximum relative displacement attained at the contact. The total energy dissipated in the system upto location x_N, as described by Eqs. (28–30) is given by (32), where $\tilde{x} = x/R^*$ and $E_t = d_0(\tilde{x}_t - \tilde{x}_1) + d_1 a \tilde{I} b \left(e^{-b\tilde{x}_1} - e^{-b\tilde{x}_t}\right) + 2d_2 \left(a\tilde{I}\right)^2 b \left(e^{-2b\tilde{x}_1} - e^{-2b\tilde{x}_t}\right)$ is the energy dissipated by the contact points in the first regime.

$$\tilde{E}_{dis} = \frac{1}{F_y \alpha_y} \int_0^\alpha (F_{load} - F_{unload})\, d\alpha$$

$$
= \begin{cases}
\left(\dfrac{3}{1.6}\right)\dfrac{c_1}{2}\left((c_4\tilde{\alpha}+c_5)^2\,(c_4\alpha_0+c_5)^2\right) \\[2mm]
+\left(\dfrac{3}{1.6}\right)\dfrac{c_2}{c_3^2}\left(-e^{-c_3(\tilde{\alpha}-1)}\,(c_3\tilde{\alpha}+c_4+c_3c_5)\right. \\[2mm]
\left.+e^{-c_3(\alpha_0-1)}\,(c_3\alpha_0+c_4+c_3c_5)\right) \\[2mm]
+\left(\dfrac{3}{1.6}\right)\dfrac{c_1\sigma_y}{c_6+1}\left(\alpha_0^{c_6+1}-1\right) \\[2mm]
+\left(\dfrac{3}{1.6}\right)\dfrac{c_2 e^{c_3}}{c_3^{c_6+1}}\left(\Gamma\,(c_6+1,c_3)-\Gamma\,(c_6+1,c_3\alpha_0)\right) \\[2mm]
+\dfrac{2}{5}-\dfrac{\tilde{F}\,(\tilde{\alpha}-\tilde{\alpha}_R)}{n} \qquad \text{if } \alpha_0 \le \tilde{\alpha} \\[4mm]
\left(\dfrac{3}{1.6}\right)\dfrac{c_1\sigma_y}{c_6+1}\left(\tilde{\alpha}^{c_6+1}-1\right) \\[2mm]
+\left(\dfrac{3}{1.6}\right)\dfrac{c_2 e^{c_3}}{c_3^{c_6+1}}\left(\Gamma\,(c_6+1,c_3)-\Gamma\,(c_6+1,c_3\tilde{\alpha})\right) \\[2mm]
+\dfrac{2}{5}-\dfrac{\tilde{F}\,(\tilde{\alpha}-\tilde{\alpha}_R)}{n} \qquad \text{if } 1<\tilde{\alpha}<\alpha_0 \\[4mm]
0 \qquad\qquad\qquad\qquad \text{otherwise,}
\end{cases}
\tag{31}
$$

where the constants c_i are as defined in Sect. 2 and $\Gamma(.,.)$ is the Gamma function. The total energy dissipation is

$$
\frac{4E_{tot}}{F_y\alpha_y} = \begin{cases}
d_0\,(\tilde{x}_N-\tilde{x}_1)+d_1 a\tilde{I}b\left(e^{-b\tilde{x}_1}-e^{-b\tilde{x}_N}\right) \\[2mm]
+2d_2\left(a\tilde{I}\right)^2 b\left(e^{-2b\tilde{x}_1}-e^{-2b\tilde{x}_N}\right), \quad \text{if } \tilde{x}_N<\tilde{x}_t \\[3mm]
E_t+d_0(\tilde{x}_N-\tilde{x}_t)+d_1 C\tilde{I}\ln\left(\dfrac{x_N}{x_t}\right) \\[2mm]
-d_2\left(C\tilde{I}\right)^2\left(\dfrac{1}{\tilde{x}_N}-\dfrac{1}{\tilde{x}_t}\right), \quad \text{otherwise.}
\end{cases}
\tag{32}
$$

References

1. Nesterenko, V.F.: Dynamics of Heterogeneous Materials. Springer, New York (2001)
2. Sen, S., Hong, J., Bang, J., Avalos, E., Doney, R.: Solitary waves in the granular chain. Physics Reports **462**(2), 21 (2008)
3. Awasthi, A.P., Smith, K.J., Geubelle, P.H., Lambros, J.: Propagation of solitary waves in 2D granular media: a numerical study. Mech. Mater. **54**, 100 (2012)
4. Manjunath, M., Awasthi, A., Geubelle, P.H.: Wave propagation in 2D random granular media. Phys. D Nonlinear Phenom. (2013, in press)
5. Johnson, K.: Contact Mechanics. Cambridge University Press, Cambridge (1985)
6. Thornton, C.: Coefficient of restitution for collinear collisions of elastic-perfectly plastic spheres. J. Appl. Mech. **64**(2), 383 (1997)
7. Wang, E., Geubelle, P.H., Lambros, J.: An experimental study of the dynamic elasto-plastic contact behavior of metallic granules. J. Appl. Mech. **80**(2) 021009 (2013)
8. Abbot, E.J., Firestone, F.A.: Specifying surface quality: a method based on accurate measurement and comparison. Mech. Eng. **55**, 569 (1933)
9. Zhao, Y., Maletta, D.M., Chang, L.: An asperity microcontact model incorporating the transition from elastic deformation to fully plastic flow. J. Tribol. **122**(1), 86 (2000)
10. Vu-Quoc, L., Zhang, X.: An elasto-plastic contact force displacement model in the normal direction: displacement-driven version. Proc. Roy. Soc. Lond. A **455**(1991), 4013 (1999)
11. Kogut, L., Etsion, I.: Elastic-plastic contact analysis of a sphere and a rigid flat. J. Appl. Mech. **69**(5), 657 (2002)
12. Jackson, R.L., Green, I.: A finite element study of elasto-plastic hemispherical contact against a rigid flat. J. Tribol. **127**(2), 343 (2005)
13. Nesterenko, V.: Propagation of nonlinear compression pulses in granular media. J. Appl. Mech. Tech. Phys. **24**(5), 733 (1983)
14. Vergara, L.: Model for dissipative highly nonlinear waves in dry granular systems. Phys. Rev. Lett. **104**(11), 118001 (2010)
15. Rosas, A., Romero, A.H., Nesterenko, V., Lindenberg, K.: Observation of two-wave structure in strongly nonlinear dissipative granular chains. Phys. Rev. Lett. **98**(16), 164301 (2007)
16. Rosas, A., Romero, A.H., Nesterenko, V., Lindenberg, K.: Short pulse dynamics in strongly nonlinear dissipative granular chains. Phys. Rev. E **78**(5), 051303 (2008)
17. Carretero-Gonzalez, R., Khatri, D., Porter, M.A., Kevrekidis, P.G., Daraio, C.: Dissipative solitary waves in granular crystals. Phys. Rev. Lett. **102**(2), 024102 (2009)
18. Khatri, D., Ngo, D., Daraio, C.: Highly nonlinear solitary waves in chains of cylindrical particles. Granul. Matter **14**(1), 63 (2012)
19. Nguyen, N.S., Brogliato, B.: Shock dynamics in granular chains: numerical simulations and comparison with experimental tests. Granul. Matter **14**(3), 341 (2012)
20. Manciu, M., Sen, S., Hurd, A.J.: Impulse propagation in dissipative and disordered chains with power-law repulsive potentials. Phys. D Nonlinear Phenom. **157**(3), 226 (2001)
21. Manjunath, M., Awasthi, A.P., Geubelle, P.H.: Wave propagation in random granular chains. Phys. Rev. E **85**(3), 031308 (2012)